

Review

# A Review of the Latest Developments in the Field of Refractory High-Entropy Alloys

Muthe Srikanth <sup>1,†</sup> , A. Raja Annamalai <sup>1,†</sup> , A. Muthuchamy <sup>2</sup> and Chun-Ping Jen <sup>3,\*</sup> 

<sup>1</sup> Centre for Innovative Manufacturing Research, VIT, Vellore 632 014, Tamil Nadu, India; muthe.srikanth@vit.ac.in (M.S.); Raja.annamalai@vit.ac.in (A.R.A.)

<sup>2</sup> Department of Metallurgical and Materials Engineering, National Institute of Technology Tiruchirappalli, Tiruchirappalli 620 015, Tamil Nadu, India; muthuchamy@nitt.edu

<sup>3</sup> Department of Mechanical Engineering and Advanced Institute of Manufacturing for High-Tech Innovations, National Chung Cheng University, Chia-Yi 62102, Taiwan

\* Correspondence: chungpingjen@alum.ccu.edu.tw

† Equally contributed as 1st Author.

**Abstract:** This review paper provides insight into current developments in refractory high-entropy alloys (RHEAs) based on previous and currently available literature. High-temperature strength, high-temperature oxidation resistance, and corrosion resistance properties make RHEAs unique and stand out from other materials. RHEAs mainly contain refractory elements like W, Ta, Mo, Zr, Hf, V, and Nb (each in the 5–35 at% range), and some low melting elements like Al and Cr at less than 5 at%, which were already developed and in use for the past two decades. These alloys show promise in replacing Ni-based superalloys. In this paper, various manufacturing processes like casting, powder metallurgy, metal forming, thin-film, and coating, as well as the effect of different alloying elements on the microstructure, phase formation, mechanical properties and strengthening mechanism, oxidation resistance, and corrosion resistance, of RHEAs are reviewed.

**Keywords:** refractory high-entropy alloys (RHEAs); powder metallurgy; casting; thin film; coatings; mechanical properties; oxidation resistance; corrosion resistance



**Citation:** Srikanth, M.; Annamalai, A.R.; Muthuchamy, A.; Jen, C.-P. A Review of the Latest Developments in the Field of Refractory High-Entropy Alloys. *Crystals* **2021**, *11*, 612. <https://doi.org/10.3390/cryst11060612>

Academic Editors: Patrice Berthod and Cyril Cayron

Received: 25 March 2021  
Accepted: 24 May 2021  
Published: 28 May 2021

**Publisher's Note:** MDPI stays neutral with regard to jurisdictional claims in published maps and institutional affiliations.



**Copyright:** © 2021 by the authors. Licensee MDPI, Basel, Switzerland. This article is an open access article distributed under the terms and conditions of the Creative Commons Attribution (CC BY) license (<https://creativecommons.org/licenses/by/4.0/>).

## 1. Introduction

In day-to-day life, the demand for new materials is greatly expanding for various applications. Different materials have been developed to increase the ability to withstand challenging environments, efficiency, and safety of materials. Refractory high-entropy alloys were developed in 2010 [1] with the primary purpose of withstanding high temperatures and to act as replacements for Ni-based superalloys and other applications, such as anodes for X-ray production gas turbine blades, armor, aerospace, and structural applications [2]. From the thermodynamic perspective, configurational entropy increases with an increasing number of elements, leading to high-entropy alloys (HEAs) [3]. The presence of multiple HEA elements leads to a decreased diffusion rate and an increased lattice distortion, which results in high-temperature stabilized phases, thus making HEAs useful for high-temperature applications [4].

Refractory elements like rhenium (Re), tungsten (W), molybdenum (Mo), tantalum (Ta), Niobium (Nb), and zirconium (Zr) are the main constituents of HEAs; along with them, other metals and materials are being used for the production of alloys named refractory high-entropy alloys (RHEAs). These alloys consist of multiple elements, and multiple elements have different crystal structures, such as face-centered cubic (FCC), body-centered cubic (BCC), hexagonal close-packed (HCP), and intermetallic compounds (B2, L1<sub>2</sub>, C14, and C15). The atomic positions of some intermetallic compounds are explained as follows. In the B2 intermetallic compound, the atomic position is the same as the body-centered cubic structure, but one type of atom occupies body-centered positions and another type of

atom occupies body corner positions, e.g., FeAl, NiAl, and CaCl. The  $L1_2$  phase atomic position is the same as that of face-centered cubic structure, but one type of atom occupies face-centered positions and another type of atom occupies body corner positions, e.g.,  $Ni_3Al$ ,  $Cu_3Al$ , and  $Al_3Zr$ . When the atomic size ratio is between 1.05 and 1.67, a Laves phase, which is an  $AB_2$  structure, is formed. There are three types of Laves phases: hexagonal (C14), cubic (C15), and hexagonal (C36). In Laves phases, the A type of atom occupies a diamond, hexagonal diamond, or related structure. The B type of atom occupies a tetrahedral void position around the A type. The sigma ( $\sigma$ ) phase is mainly observed in stainless steels and Cr-containing alloys; it has a tetragonal structure, e.g., equiatomic FeCr, CoCr, and FeMo [5,6].

RHEAs are specialized materials, and researchers are constantly developing new RHEA alloys and fabrication techniques. This paper reviews recent developments in RHEAs, such as processing techniques, structural properties, welding, thin films, coatings, oxidation, corrosion behavior, and computational methods.

## 2. Processing Techniques

The manufacturing process of RHEAs is crucial because of the high melting point and considerable variation of alloying element melting points. This produces the segregation and evaporation of low-melting-point elements and less bonding; overcoming these problems in the manufacturing of RHEAs is difficult [7]. All alloys' mechanical properties are based on the manufacturing process, including vacuum arc melting, induction melting, additive manufacturing, hot isostatic pressing, and spark plasma sintering. The selection of the manufacturing process depends on the alloying elements and their application. This section is mainly focused on new developments in fabrication techniques in refractory high-entropy alloys. One manufacturing process that was recently under development is spark plasma sintering, and many newer processes have proven their efficiency.

The NbMoTaWVTi refractory high-entropy alloy manufactured by spark plasma sintering showed better mechanical properties than an as-cast NbMoTaWVTi alloy [8]. An ultrafine grain microstructure was formed in an MoNbTaTiV high-entropy alloy fabricated by mechanical alloying followed by spark plasma sintering [9]. Uniformly distributed nanosized TiC dispersoids were found to be formed in  $Nb_{42}Mo_{20}Ti_{13}Cr_{12}V_{12}Ta$  RHEA that underwent spark plasma sintering. Additionally, an  $Nb_{42}Mo_{20}Ti_{13}Cr_{12}V_{12}Ta$  RHEA showed good mechanical properties [10]. When fabricated using laser metal deposition, cracks were formed in an NbMoTaW high-entropy alloy [11]. An NbMoTaW alloy can be successfully fabricated using a laser cladding deposition process without cracks; finer grain and dendrite sizes have been observed in this process due to its fast solidification [12].

Making an alloy with low- and high-melting-point elements was previously challenging to fabricate. Dobbstein et al. reported that a TiZrNbHfTa alloy could be successfully fabricated using the in situ alloying of elemental powder the sequential laser metal deposition (LMD) and re-melting steps to get better results for low and high melting point powders [13]. Because of a massive difference in Ti's and Ta's melting points, the fabrication of a TiZrNbTa alloy is complex, but it can now be successfully fabricated using the LMD process, which has shown promising results [14]. First-time, single-phase, carbide, high-entropy ceramics ( $Hf_{0.2}Ta_{0.2}Ti_{0.2}Nb_{0.2}Mo_{0.2}$  and  $Zr_{0.2}$ )C were fabricated by self-propagating high-temperature synthesis using spark plasma sintering [15]. An MoNbTaW refractory high-entropy alloy can be successfully fabricated with a laser-based additive manufacturing process [16]. An ultra-hard and nanocrystalline (average grain size: 5.9 nm) BCC-structured, VNbMoTaW high-entropy alloy can be fabricated using powder metallurgy and mechanical alloying followed by sintering—this alloy has an extraordinary hardness (11.4 GPa) that twice that of the coarse grain structure [17].

## 3. Microstructure and Phases

For each material to achieve its required mechanical properties, microstructure and phase formation is essential. The primary manufacturing process involved in high-entropy

alloys is vacuum arc melting [18]. Segregation, dendrite size, and grain size are difficult to control in the casting process, so many of studies have used a powder metallurgy process to avoid these problems [8,15,17]. After the mechanical milling of powders, MoNbTaTiV refractory high-entropy alloy powders showed nanocrystalline grains with a BCC phase and homogeneous distribution of the elements, and after annealing at 1200 °C, nanosized grains and a BCC crystal structure were preserved. This experiment showed that this alloy has a high phase and thermal stability of 1200 °C [19].

To increase room temperature ductility, Senkov et al. developed an HfNbTaTiZr RHEA. It has a high room temperature ductility, but it suffers from high-temperature yield strength [20]. To improve the yield strength above 1200 °C, another study was done on the microstructure and phase formation; an HfNbTaTiZr alloy was fabricated using arc melting and an as-cast structure containing nanoprecipitates in a BCC matrix were formed. After annealing at 1000 °C, an HCP-1 phase formed; as the annealing temperature increased to 1200 °C, the HCP-1 phase dissolved; when the annealing temperature increased up to 1400 °C, the HCP-1 phase wholly disappeared and nanoprecipitate formed; and at 1450 °C, the annealed alloy microstructure contained two new FCC phases, an HCP-2 phase and nanoprecipitate that was still in the BCC matrix. This type of microstructure gives this alloy better mechanical properties, even at high temperatures (for full details, refer to [21]). Computational studies reported that the BCC phase was transferred into an HCP structure in Hf-containing alloys; this was experimentally proven by Cheng Yang et al. and Senkov et al. [21,22].

In high-entropy alloys, the mechanical properties are enhanced by reinforcement techniques. Carbon reinforcement enhances thermal stabilization, creep resistance, and ultra-high temperature strength with carbide phase formation [23]. Recent work has been done on CrMoNbWTi-C refractory high-entropy alloys. After mechanical alloying, the BCC solid solution was hot-pressed to get an intermetallic Cr<sub>2</sub>Nb phase and high-temperature (Ti and Nb)C. Due to carbide and intermetallic compounds, the yield strength and high-temperature stability were found to be increased [24,25]. Senkov et al. reported that Al addition increased the alloy's strength, which they demonstrated in an NbNiTaTiW refractory high-entropy alloy [26]. According to Senkov et al., the addition of 10 atomic % Al to the NbNiTaTiW alloy led to an increase in hardness due to the decrease in the dendrite size, with both alloys (NbNiTaTiW and NbNiTaTiWAl) showing effect in hardness after heat treatment, and as the soaking time was increased up to 72 h, the hardness (the Vickers's hardness values of both alloys are shown in Table 1) was increased due to the increasing the volume fraction of the L1<sub>2</sub> phase [27].

**Table 1.** Vickers hardness of as-cast and heat-treated refractory high-entropy alloys (RHEAs) (NbNiTaTiW and NbNiTaTiWAl) [27].

Sample Condition	NbNiTaTiW (Hv)	NbNiTaTiWAl (Hv)
As cast	410	578
1000 °C for 24 h	435	673
1000 °C for 48 h	439	632
1000 °C for 72 h	432	637

After radiation exposure, no phase change was observed in HfNbTaTiZr RHEA, and this study experimentally showed that HfNbTaTiZr RHEA has excellent resistance to radiation, so this material is suitable to use in radiation [28]. An Al<sub>20</sub>Cr<sub>10</sub>Nb<sub>15</sub>Ti<sub>20</sub>V<sub>25</sub>Zr<sub>10</sub> refractory high-entropy alloy was found to have a hypoeutectic composite-like structure that contained B2 and C14 Laves regions and a B2 eutectic region. After annealing the Al<sub>20</sub>Cr<sub>10</sub>Nb<sub>15</sub>Ti<sub>20</sub>V<sub>25</sub>Zr<sub>10</sub> RHEA at 1200 °C, the Zr<sub>5</sub>Al<sub>3</sub>, B2, and C14 phases were formed, thus giving extra strength to the material; the microstructure of the Al<sub>20</sub>Cr<sub>10</sub>Nb<sub>15</sub>Ti<sub>20</sub>V<sub>25</sub>Zr<sub>10</sub> alloy is shown in Figure 1 [29]. Segregation is the main problem in as-cast alloys in the case of refractory high-entropy alloys. A TaNbVTiAlx alloy was fabricated using a powder met-

allurgy process, which resulted in a single-phase BCC solid solution with no segregation in the microstructure, a uniform microstructure throughout the alloy, and better mechanical properties [30]. When fabricating an NbTaTiV refractory high-entropy alloy using powder metallurgy sintering at above 1700 °C, porosity and segregation were not observed [31].

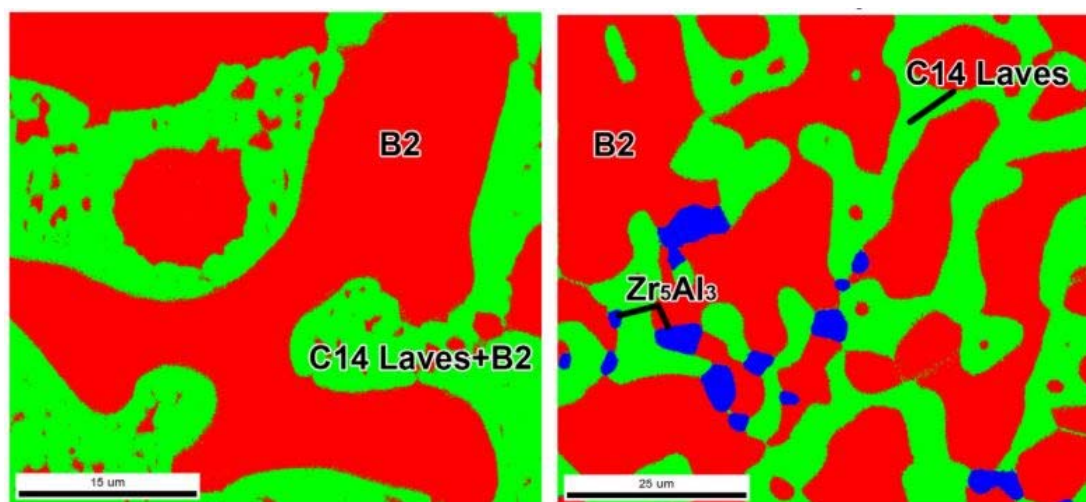


Figure 1.  $\text{Al}_{20}\text{Cr}_{10}\text{Nb}_{15}\text{Ti}_{20}\text{V}_{25}\text{Zr}_{10}$  alloy microstructure of alloy as cast (left side) and after annealing (right side) [29].

A novel and lightweight CrNbTiZrAl<sub>x</sub> RHE alloy was developed to study the effect of aluminum addition. Al addition transformed the microstructure from a hypoeutectic and eutectic alloy to a hypereutectic alloy, and the hypereutectic alloy had a high strength-to-weight ratio [32]. Additionally, Ti's addition to an NbMoTaW refractory high-entropy alloy increased its high-temperature stability by forming a stable single BCC structure up to its melting point [33]. Rhenium (Re) is a refractory element with a high melting point of 3185 °C, and Ni-base superalloys help improve the creep resistance of Re [34,35]. Yusenko et al. reported that RHEAs with added Re had a high stability at extreme temperatures [36]. Another study was done on an ReTaWNbMo RHEA, and it was shown that as-cast alloys had a BCC crystal structure after annealing, but with increasing annealing temperature (673 K (400 °C), 873 K (600 °C), 1073 K (800 °C), and 1273 K (1000 °C)), coarse dendrites were transformed into equiaxed grains [37]. When Al was added to the  $\text{Mo}_{0.5}\text{NbTa}_{0.5}\text{TiZr}$  RHEA, an ordered precipitate formed in the Ti-Zr rich matrix without Al disorder precipitates forming [38].

#### 4. Mechanical Properties

##### 4.1. Mechanical Behavior

$\text{Ti}_{(50 - 1.5625x)}\text{Nb}_{(30 - 0.9375x)}\text{CrVNi}_{(1.5x)}\text{Al}_x$  ( $x$ : 0, 5, 7, and 10,) alloys with varying aluminum contents were subjected to tensile tests at room temperature and 800 °C to find their yield strength and ultimate tensile strength (as shown in Table 2). In a  $\text{Ti}_{34.4}\text{Nb}_{20.6}\text{Cr}_{10}\text{V}_{10}\text{Ni}_{15}\text{Al}_{10}$  ( $X = 10$ ) alloy, Ti and Nb's gradual replacement with Al and Ni resulted in the formation of coarse Ti, Ni-rich sigma, and  $\text{Ti}_2\text{Ni}$  phases. These BCC, sigma, and  $\text{Ti}_2\text{Ni}$  phases were found to improve the material's mechanical characteristics, and the nanoindentation of those phases is shown in Table 3 [39]. Panina et al. reported that yield strength and ultimate tensile strength improved after replacement [39]. NbTaTiV refractory high-entropy alloys were synthesized using powder metallurgy as the sintering temperature was increased from 1500 to 1700 °C, and the Vickers hardness increased (as shown in Figure 2) [31]. This report demonstrated that the powder metallurgy as-sintered alloy had a higher Vickers hardness than the as-cast alloy, and as the sintering temperature increased, segregations disappeared, pores were eliminated, a homogeneous microstructure was formed, and a 99.5% relative sintered density was achieved. NbMoTaW and NbMoTaWV were two refractory high-entropy alloys first developed by Senkov et al. [1]. These two alloys have high

yield strengths, even at high temperatures, but at room temperature, they are brittle [40]. Ti was added to the NbMoTaW alloy to overcome this problem, and it enhanced the ductility from 1.9 to 11.5% and increased yield strength to up to 1455 MPa. This alloy had a stable microstructure up to the melting point, and adding Ti made the alloy highly ductile. This alloy is suitable for high-temperature applications due to its combination of high ductility, yield strength, and high-temperature phase stability [33].

**Table 2.** Yield strength and ultimate strength of TiNbCrVNiAlx alloys at room temperature and 800 °C [39].

Alloy	Yield Strength (MPa)	Ultimate Tensile Strength (MPa)
<b>At Room Temperature</b>		
X = 0	755	-
X = 5	775	1135
X = 7	1270	1685
X = 10	-	1395
<b>At 800 °C</b>		
X = 0	45	60
X = 5	85	105
X = 7	110	200
X = 10	285	395

**Table 3.** The hardness of different phases measured by the nanoindentation method [39].

Phase	Hardness (Hv)
BCC	530
Ti <sub>2</sub> Ni	935
Sigma phase	1085

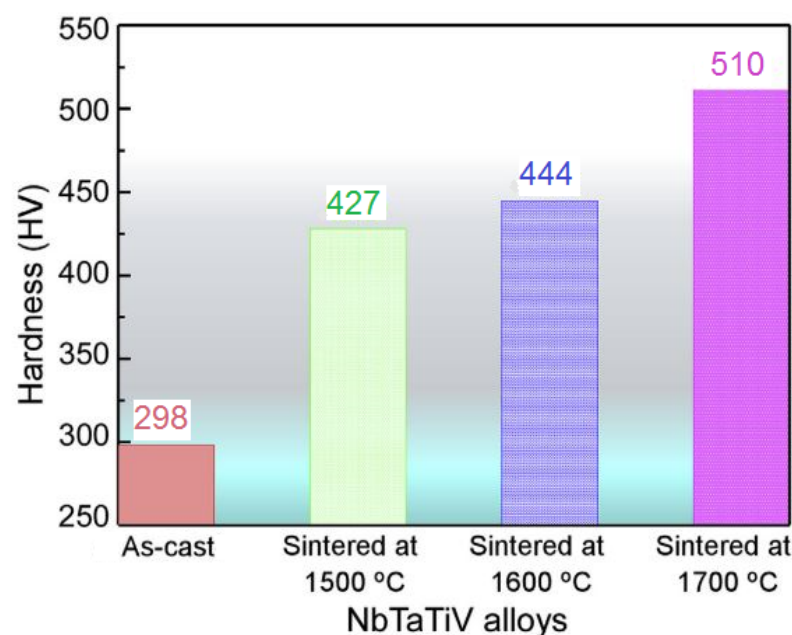


**Figure 2.** The hardness of an as-cast and powder metallurgy-produced NbTaTiV RHE alloy sintered at 1500, 1600, and 1700 °C [31].

Tungsten and molybdenum were added to an HfNbTaTiZr alloy to improve its high-temperature properties. The mechanical properties of HfNbTaTiZr, HfNbTaTiZrW, and HfNbTaTiZrWMo alloys were studied. Compared with the HfNbTaTiZr alloy, the HfNbTaTiZrW and HfNbTaTiZrWMo alloys had higher tensile strength, better high-temperature stability, and no new phase formation up to 1200 °C [41]. For an HfMoNbTiVZr alloy, increasing the Mo and Zr contents yielded a strength increase, whereas increasing the Ti content yielded a strength decrease. Shafiei Ali reported that Ti's presence in this NbMoTaW alloy increased its strength, but its presence in an Hf-containing alloy decreased the strength; for more details, refer to [42]. As Al content increased in an Al<sub>x</sub>MoNbTaTiV alloy, the lattice constant decreased from 3.211 to 3.100 Å, yield strength increased from 1228 to 1391 MPa, and hardness increased from 421 to 578 Hv [43].

Equiatomic NbMoTaWVCr refractory high-entropy alloys fabricated by mechanical alloying followed by spark plasma sintering at 1400–1700 °C were studied. After sintering the (Cr and V)<sub>2</sub>, (Ta and Nb) Laves phase, Ta<sub>2</sub>VO<sub>6</sub> particles were precipitated from the BCC matrix. The as-sintered alloy had a yield strength of 3416 MPa, 5.3% plastic strain, and a Vickers hardness of 9908 MPa; this alloy was found to have ultra-high strength and hardness compared to other alloys. If sintered above 1500 °C, the grain size increased and the strength decreased [44]. After irradiation, a coarse-grained and nanocrystalline TiZrNbHfTa refractory high-entropy alloy had an increased hardness (shown in Table 4) and increased yield strength without decreased ductility; it was observed that the radiation-induced hardening created a lattice defect. This review demonstrated that this alloy has excellent damage tolerance before and after irradiation, making it suitable for IV-generation nuclear reactor applications [45]. A TiAlVNbMo refractory high-entropy alloy was shown to have a lower density (~6 g/cm<sup>3</sup>) than other refractory high-entropy alloys and nickel-based superalloys, and it also had high strength and good plasticity at high temperatures (1000 °C) [46].

**Table 4.** Mechanical properties of an unirradiated and irradiated RHEA [45].

	Yield Strength (MPa)	Ultimate Strength (MPa)	Elastic Modulus (GPa)
Unirradiated (avg)	1833	2106	78.5
Irradiated (avg)	2088	2475	104.7
% of radiation induced increment	13.9%	17.5	33.4

An aluminum-containing high-entropy alloy (Al<sub>10</sub>Nb<sub>1.5</sub>Ta<sub>5</sub>Ti<sub>30</sub>Zr<sub>40</sub>), as-cast after annealing at 1100 °C and quenched in water, gave almost the same yield strength (1050 MPa) at room temperature and compression ductility over 50%. In contrast, after annealing up to 600 °C, the yield strength of the same alloy (Al<sub>10</sub>Nb<sub>1.5</sub>Ta<sub>5</sub>Ti<sub>30</sub>Zr<sub>40</sub>) was drastically decreased to 250 MPa [47]. In this study, Senkov et al. demonstrated that aluminum-containing refractory high-entropy alloys' mechanical properties depend on temperature. Another work was done to study the mechanical properties of an as-quenched equiatomic refractory high-entropy alloy at four annealing temperatures (673 K (400 °C), 873 K (600 °C), 1073 K (800 °C), and 1273 K (1000 °C)), ultimately showing that as the annealing temperature increased, yield strength, compressive plasticity, and fracture strength improved [37].

#### 4.2. Strengthening Mechanism

Recent work was done on an HfTaTiVZr refractory high-entropy alloy based on the strain rate sensitivity of the thermally-activated deformation mechanism, a significant problem in next-generation nuclear applications. This study concluded that changes in strain rate sensitivity depend on the sample's loading state and surface-to-volume ratio. [48]. An NbTiHfZr high-entropy alloy has a BCC crystal structure with a small amount of the HCP phase. After cold working and annealing, the HCP nanoprecipitate volume

fraction increased, thus improving strength and ductility [49]. A study was performed on an  $\text{MoNbRe}_{0.5}\text{W}(\text{TaC})_x$  composite refractory high-entropy alloy with varying TaC contents. The addition of TaC to the alloy increased the metal carbide phase but decreased the BCC matrix volume fraction; because of the formation of MC carbides, the  $\text{MoNbRe}_{0.5}\text{W}(\text{TaC})_{0.6}$  alloy obtained the highest mechanical properties, including Vickers hardness (615 Hv) and yield strength (1245 MPa) [50]. During the hot forging of an as-sintered RHEA ( $\text{TiNbTa}_{0.5}\text{ZrAl}_{0.5}$ ), Zr and Al-rich HCP precipitates were formed in the BCC matrix, which was further strengthened by annealing at 1000 °C for 2 h. After annealing, the compressive yield strength improved to 1740 MPa at a compressive strain of 20% [51]. A new type of refractory high-entropy alloy, NbMoTaW, was developed using mechanical alloying followed by spark plasma sintering; this alloy consisted of metallic and non-metallic compounds. Ta attracted  $\text{O}_2$  and C, thus forming oxides and carbides, respectively. Nonmetal compounds acted as reinforcements in the matrix, resulting in a high hardness of 892 Hv and a compressive strength of 1630 MPa, even at 800 °C. From the results, Roh et al. reported that these alloys were suitable for high-temperature applications [52].

An HfNbTaZrTi refractory high-entropy alloy was cold-rolled and annealed at 1000–1200 °C, and recrystallization and grain growth kinetics were investigated. At 1000–1100 and 1100–1200 °C, activation energy was reported as 205 and 401 KJ/mol, respectively. Chen et al. reported that a higher activation energy for grain boundary migration occurred due to Ta and Nb [53]. During the high temperature (1000 °C) compression test of an HfNbTaTiZr RHEA, the bulging, dynamically recrystallized (DRX) grain was formed. The fraction of the DRX structure increased with the strain rate. DRX grains were deformed by grain boundary sliding (GBS) [54].

#### 4.3. Mechanical Deformation Mechanism

A new class of non-equiatomic low-density refractory alloys ( $\text{Ti}_{89}\text{CrNbV}_{0.56}$ ) was investigated by Yurchenko et al. Generally, refractory high-entropy alloys are challenging to work in a cold environment because of their low ductility at room temperature. However, the  $\text{Ti}_{89}\text{CrNbV}_{0.56}$  alloy is cold, with a ductility of up to 80% in room temperature conditions; after the 80% cold working, a dislocation substructure kink and shear bands were formed. This was attributed to the increases in Vickers hardness (450–469 Hv), yield strength (1020 MPa), and ultimate strength (1535 MPa). After annealing at 800 °C, a Cr-rich FCC (C14) Laves precipitate was formed. Recovery and recrystallization were observed between 800 and 1200 °C, and the effect of annealing on hardness is shown in Figure 3 [55].

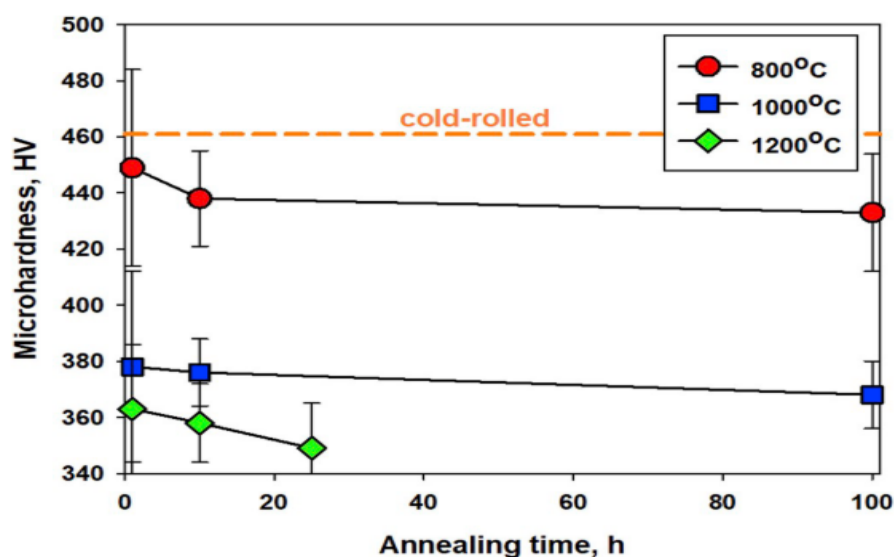


Figure 3. Effect of annealing time and temperature on the hardness of a  $\text{Ti}_{89}\text{CrNbV}_{0.56}$  alloy [55].

A study was done using a three-stage (0–15%, 15–40%, and 40–80%) cold rolling process up to 80% on an HfNbTaTiZr RHEA. The authors reported that in the first stage (0–15%), dislocation density increased; in the second stage (15–40%), kink bands formed; and in the last stage (40–80%), shear bands with fine lamellar substructures formed. Overall, this resulted in a yield strength of 1220 MPa [56].

## 5. Welding

A new study was done on employing refractory high-entropy alloys in the welding process. There have been many studies on welding high-entropy alloys, but no studies on the welding of refractory high-entropy alloys are available in the literature. Only one study was done on  $\text{Ti}_{1.89}\text{NbCrV}_{0.56}$  RHEAs welded in different conditions using a laser beam welding process. Panina et al. reported that room-temperature laser beam welding on a  $\text{Ti}_{1.89}\text{NbCrV}_{0.56}$  alloy created hot cracks due to its low ductility. To overcome the hot cracking problem, preheating was carried out between 600 and 800 °C. This provided sound butt joint welds. As the preheating temperature increased, the grain size increased, as shown in Figure 4 [57].

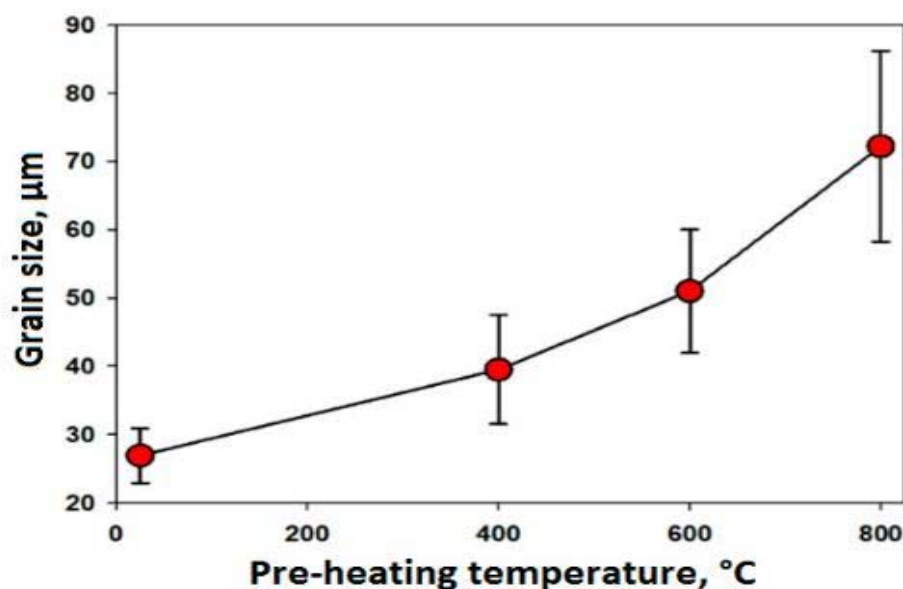


Figure 4. Effect of the preheating temperature on grain size on a  $\text{Ti}_{1.89}\text{NbCrV}_{0.56}$  alloy [57].

## 6. Thin Films

Higher melting point, high thermal stability, less diffusivity, high hardness, and high damage tolerance properties are expected, and RHEAs can be used in demanding environments. RHEA properties allow them to be used as coatings on standard materials. Using thin-film technology, RHEA thin films have been developed for next-generation materials in high-temperature applications. An NbMoTa RHEA thin film was developed using direct current (DC) magnetron sputtering by sintering a mixture of multi-elemental powders; this thin film was found to have a nanocrystalline grain solid solution phase with a BCC structure. In their investigation, Kim et al. reported that these thin films had a hardness of 12 GPa and an electrical resistivity of 168  $\mu\Omega\text{cm}$ , so they could be used as hard coatings for protective layers and nanosized electrical resistors for electronic circuits [58]. Matheus A. Tunes et al. developed an NbTaMoW equiatomic, refractory high-entropy thin film using an ion beam sputtering deposition technique, and this thin film nanoindentation had a hardness of 22.8 GPa, high nanoscratch resistance, high crack propagation resistance, and high delaminating resistance; the combination of all these properties allows this thin film to be used as a coating on other materials in extreme environments [59].

## 7. Coatings

An  $\text{MoFe}_{1.5}\text{CrTiWAlNb}_x$  refractory high-entropy alloy was coated on M2 tool steel using laser cladding technology. This coating was found to contain a BCC, metal carbide, and C14 Laves phase with an increase in niobium content, wear resistance, and increased micro-Vickers hardness compared to a control, and it reached a maximum of 910  $\text{Hv}_{0.2}$  [60]. Further work was done to study the RHEA's microstructure, phase stability, and mechanical properties at high temperatures. The high-temperature experiment showed no change in the dendrites and MC carbides in the 800 °C-annealed material. Below 700 °C, annealing resulted in a slight increment in wear resistance and hardness. Another benefit of this coating was a dense and highly thermally stable oxide formed at 800 °C, which was found to have a better oxidation resistance than M2 high-speed steel [61].

## 8. Oxidation Behavior

Refractory high-entropy alloys have admirable mechanical properties at high temperatures, and the oxidation behavior of these alloys is crucial. These alloys have greater oxidation resistance than Ni-base superalloys. Many research studies are currently investigating the oxidation behavior of refractory high-entropy alloys at different temperatures and conditions. A study was performed on the high-temperature oxidation behavior of three alloys,  $\text{TiNbTa}_{0.5}\text{Zr}$ ,  $\text{TiNbTa}_{0.5}\text{ZrAl}$ , and  $\text{TiNbTa}_{0.5}\text{ZrAlMo}_{0.5}$ ; the addition of aluminum to the  $\text{TiNbTa}_{0.5}\text{Zr}$  alloy led to the formation of  $\text{Al}_2\text{O}_3$ , which has a good adherence with the  $\text{TiNbTa}_{0.5}\text{ZrAl}$  substrate, whereas the addition of Mo to this alloy decreased the oxidation resistance because when  $\text{MoO}_3$  is formed, it evaporates at high temperatures and leaves pores and cracks [62]. An  $\text{Al}_{10}\text{CrMo}_x\text{NbTiZr}_{10}$  alloy was subjected to a high temperature of 1000 °C for 50 h in normal air, and the oxide layer disintegrated after 10 h because of the molybdenum content. Another  $\text{Al}_{10}\text{CrNbTiZr}_{10}$  alloy with 0% molybdenum was subjected to the same conditions, and the oxide layer in this alloy did not disintegrate after 50 h. The oxide layers thus formed were  $\text{CrNbO}_4$ ,  $\text{Al}_2\text{O}_3$ , and  $\text{AlTiO}_5$ . It was reported that an alloy with 0% Mo had the high oxidation resistance and could be used for high-temperature applications [63]. The  $\text{MoO}_3$  oxide layer is not suitable for high-temperature applications. After 100 h of the oxidation of an  $\text{Al}_{20}\text{Nb}_{30}\text{Ta}_{10}\text{Ti}_{30}\text{Zr}_{10}$  refractory complex concentrated alloy (RCCA), the outer layer had a composition of  $\text{NbAlO}_4$ ,  $\text{ZrO}_2$ ,  $\text{Ti}_7\text{Al}_2\text{O}_{15}$ , and  $\text{Ta}_2\text{Nb}_4\text{O}_{15}$ ; the middle layer contained BCC metal,  $\text{TiO}_2$ ,  $\text{ZrO}_2$ , and Al-rich oxide; and the internal oxidation layer containing BCC metal,  $\text{TiO}_2$ ,  $\text{ZrO}_2$ , and  $\text{Ta}_2\text{Al}$  slowed down the oxidation rate [64]. Three types of oxide layers,  $\text{Cr}_2\text{O}_3$ ,  $\text{Al}_2\text{O}_3$ , and  $\text{CrTaO}_4$ , were formed using a Ta, Cr, Mo, Al, and Ti combination alloy.

Four RHEAs— $\text{TaMoCrTiAl}$ ,  $\text{NbMoCrTiAl}$ ,  $\text{NbMoCrAl}$ , and  $\text{TaMoCrAl}$ —were tested at 1000 °C to find the effect of alloying elements on oxidation behavior.  $\text{Cr}_2\text{O}_3$ ,  $\text{Al}_2\text{O}_3$ , and  $\text{CrTaO}_4$  dense oxide layers formed in the  $\text{TaMoCrTiAl}$  alloy; titanium addition played a vital role in forming the  $\text{CrTaO}_4$  oxide layer through oxygen diffusion, making it withstand high temperatures and preventing oxidation. This oxide layer was found to have higher oxidation than other oxide layers ( $\text{CrNbO}_4$ ,  $\text{Al}_2\text{O}_3$ ,  $\text{Cr}_2\text{O}_3$ ,  $\text{TiO}_2$ ,  $\text{ZrO}_2$ , and  $\text{AlTiO}_5$ ). A  $\text{CrTaO}_4$  oxide layer may be helpful in future materials to protect from high temperatures.  $\text{Nb}_2\text{O}_5$  polytypes were formed in Niobium-added alloys, which created pores in the oxide layers [65].

Another study was done on an equiatomic  $\text{TaMoCrTiAl}$  alloy to determine the oxidation resistance of the  $\text{CrTaO}_4$  oxide layer at different temperatures from 1000 to 1800 °C, as shown in Figure 5. In this study, Gorr et al. reported that a  $\text{CrTaO}_4$  layer formed between 500 and 1500 °C, and this layer was highly protective against high-temperature oxidation [66]. Murakami et al. studied the high-temperature oxidation behavior of an intermetallic alloy in the  $\text{Cr}_2\text{O}_3$  and  $\text{Al}_2\text{O}_3$  oxide layers of  $\text{Cr}_{17.6}\text{Al}_{20.3}\text{Mo}_{15.2}\text{Nb}_{2.9}\text{Si}_{13.4}\text{Ta}_{5.4}\text{Ti}$  RHEA that formed at 1200 °C and evaporated at 1300 °C; mullite was formed at 1400 °C, and they found nitride particles in all oxide layers. Murakami et al. concluded that RHEAs are susceptible to nitridation and oxidation [67]. An equimolar  $\text{NbZrTiCrAl}$  refractory high-entropy alloys was found to follow the parabolic rate law between 800 and 1000 °C,

where a dense oxide layer formed with  $\text{CrNbO}_4$ ,  $\text{ZrO}_2$ ,  $\text{TiO}_2$ , and  $\text{Al}_2\text{O}_3$  and followed linear oxidation kinetics; above  $1200\text{ }^\circ\text{C}$ , it had less oxidation resistance [68]. For the first time, aluminizing was done on the ductile RHEA  $\text{Al}_{0.5}\text{Cr}_{0.5}\text{Nb}_{0.5}\text{Ta}_{0.5}\text{Ti}_{0.5}$  to increase oxidation resistance; it was reported that when using the one-step process, cracks were seen on the protective layer [69]. To strengthen the layer, a two-step process was done to give a dense layer [70].

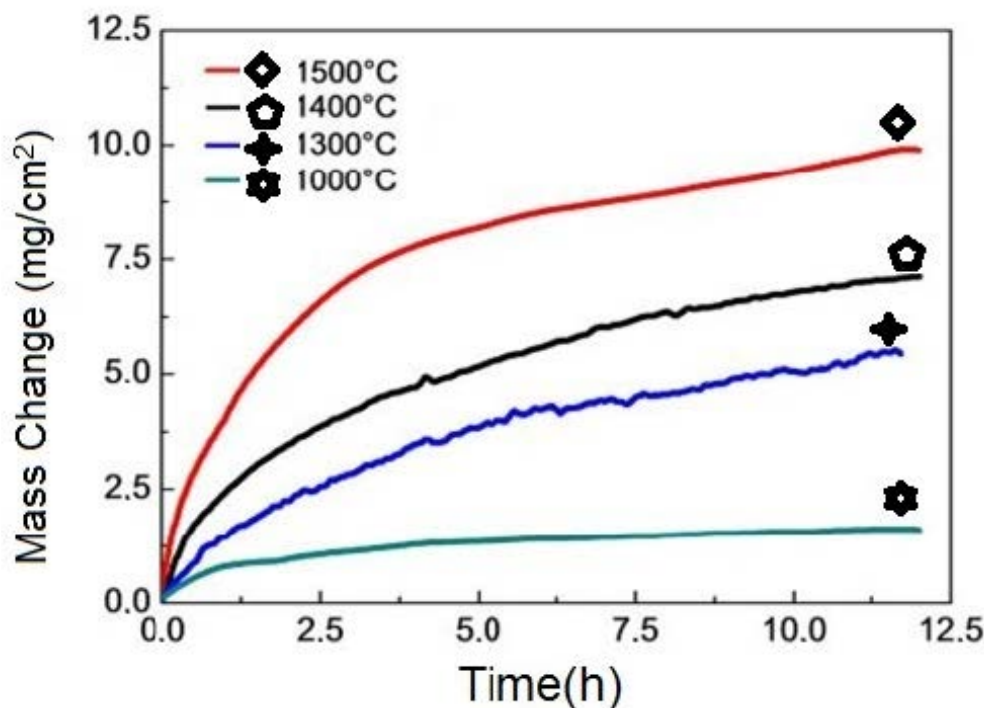


Figure 5. Oxidation curves of Ta-Mo-Cr-Ti-1 at 1000, 1300, 1400, and 1500 °C [66].

## 9. Corrosion Behavior

Corrosion is one of the most significant problems in all metals. According to a National Association of Corrosion Engineers (NACE) report in 2016 on the international measures of prevention, application, and economics of corrosion technology (IMPACT), USD 2.5 trillion (equivalent to almost 3.4% of the world's gross domestic product (GDP)), is spent on corrosion protection worldwide. This review paper discusses the latest development of corrosion studies on refractory high-entropy alloys.

The corrosion resistance of  $\text{Hf}_{0.5}\text{Nb}_{0.5}\text{Ta}_{0.5}\text{Ti}_{1.5}\text{Zr}$  RHEA was investigated in a 3.5 wt% NaCl solution, and Zhou et al. concluded from this experiment that this alloy has a higher corrosion resistance than other refractory high-entropy alloys and 316L stainless steel, as shown in Figure 6. The presence of tantalum and  $\text{OH}^-$  species makes a highly immune passive film [71]. Motallebzadeh et al. reported that  $\text{TiZrTaHfNb}$  and  $\text{Ti}_{1.5}\text{ZrTa}_{0.5}\text{Hf}_{0.5}\text{Nb}_{0.5}$  refractory high-entropy alloys are suitable for biomedical applications, with higher resistance to pitting corrosion and general corrosion than  $\text{Ti}_6\text{AlV}$ , 316L, and CoCrMo alloys. In comparing  $\text{TiZrTaHfNb}$  and  $\text{Ti}_{1.5}\text{ZrTa}_{0.5}\text{Hf}_{0.5}\text{Nb}_{0.5}$  alloys, the latter was shown to have a high corrosion resistance [72]. Another study was done to determine the corrosion behavior of ReTaWNbMo equiatomic refractory high-entropy alloys, which were annealed at different temperatures (673, 873, 1073, and 1273 K) before their corrosion behavior was tested in a 3.5 wt% NaCl solution. It was observed that when the elemental segregation was changed, charge transfer resistance was also modified, leading to a change in the corrosion resistance; all alloys annealed at 1200 K for 12 h showed a high corrosion resistance [37].

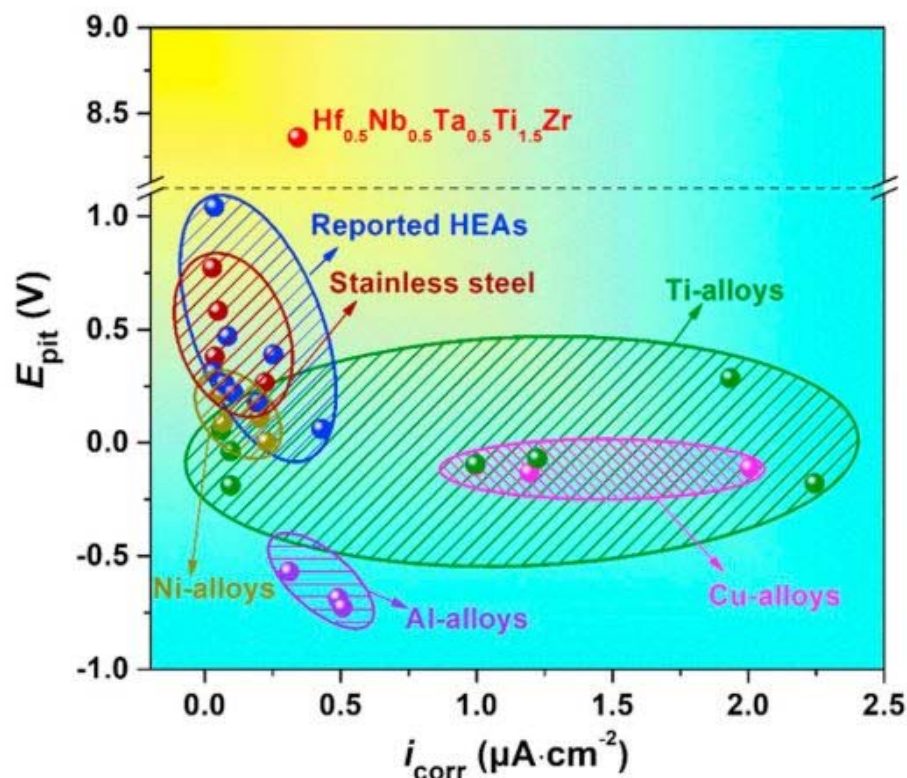


Figure 6. Compare the corrosion of an  $\text{Hf}_{0.5}\text{Nb}_{0.5}\text{Ta}_{0.5}\text{Ti}_{1.5}\text{Zr}$  RHEA with other HEAs and other alloys in a 3.5 wt% NaCl solution [71].

## 10. Computational Methods

Some of the existing refractory high-entropy alloys and future required RHEAs have been developed and modeled using the ICME software to calculate phase diagram (CALPHAD) modeling. In the CALPHAD approach, the Gibbs free energy, diffusion kinetics, phase transformation kinetics, enthalpy of formation, enthalpy of mixing, the entropy of mixing, electron valance, and atomic radius difference parameters are used to design the alloy and predict phase stability. In CALPHAD calculation the console module and TCHEA3 databases are used to design the alloy. Abheepsit Raturi et al. reported that CALPHAD and experimental results matched in the case of MoNbTaVW and CrMoReVW RHEAs [73]. CompuTherm is developing a PanNb thermodynamic database to study the phase diagrams of quaternary alloys. Raturi et al.'s work reported that BCC Mo, Ta, and V alloys below 700–1000 °C decomposed to two BCC structures, and Hf decomposed to BCC and HCP phases. An (NbTiZr)X alloy showed satisfactory results that matched the practical results [22], and, by using the first-principles calculation, elastic constant, modulus, and lattice parameter, the total energy of NbMoTaW and NbMoTaWV refractory high-entropy alloys was calculated [74]. The atomic properties were accurately predicted using bi-linear regression models [75], and some researchers have reported that iterative MATLAB could be used to design RHEAs. Using this method, Shafiei et al. generated 40,000 alloys by changing the proportion of alloying elements in the HfMoNbTaTiVZr alloy system, and they concluded that the strength of the alloy increased with the addition of zirconium and molybdenum and decreased with the addition of titanium. The strength obtained through computational modeling was almost identical to the theoretical and experimental results [42].

## 11. Summary

RHEAs have potent properties that suggest that they could have promising applications. There are different elements and manufacturing processes to develop RHEAs.

Researchers have been designing new RHE alloys and manufacturing processes to achieve better performance over the last decade. From the latest developments in the field of RHEAs from the available literature, the following summary can be made.

In manufacturing RHEAs, ball milling and mechanical milling, followed by spark plasma sintering, give the best results. Pores, cracks, and segregation can be eliminated by using the powder metallurgy process. Alloys fabricated using nanosize powders have a higher strength than alloys synthesized with coarse powders. Due to rapid localized heating, spark plasma sintered alloys have a fine grain structure.

RHEAs can be successfully fabricated using the LMD sequential melting technique. The additive manufacturing of RHEAs helps to create crack-free and segregation-free refractory high-entropy alloys.

After irradiation, due to the formation of lattice defects, yield strength is increased in the HfNbTaTiZr alloy. Alloys with tungsten and molybdenum have a high strength and high-temperature stability. Adding Ti to the NbMoTaW alloy stabilizes the BCC structures to their melting points and increases room temperature ductility from 1.9 to 11%. In the HfMoNbTaTiVZr alloy, yield strength increases as Mo and Zr content increases, and yield strength decreases as Ti content increases. In an NbMoTaWVCr alloy after SPS, a (Cr and V)<sub>2</sub> (Ta and Nb) Laves phase and Ta<sub>2</sub>VO<sub>6</sub> were found to be precipitated in the matrix, and this alloy as found to have a yield strength of 3416 MPa and a Vickers hardness of 9908 MPa. The addition of TaC to RHEAs increases the metal carbide volume fraction. RHEA properties can be altered using heat treatment.

Using laser beam welding, a Ti<sub>1.89</sub>NbCrV<sub>0.56</sub> refractory high-entropy alloy welded at room temperature had hot crack formation, but it was successfully welded in preheating conditions without any cracks.

NbMoTaW RHEA thin films have been developed using direct current magnetic sputtering and ion beam technology. These thin films have a high hardness (12 GPa), scratch resistance, and delaminating resistance. These films can be used in hard nanocoatings and nanoelectronic circuits. RHEA coatings are done on the metal surface, and these coatings are used for hard facing, high-temperature oxidation resistance, as well as corrosion resistance.

When Ta, Cr, Mo, Al, Nb, and Ti are added, dense Cr<sub>2</sub>O<sub>3</sub>, Al<sub>2</sub>O<sub>3</sub>, MoO<sub>3</sub>, Nb<sub>2</sub>O<sub>5</sub>, and CrTaO<sub>4</sub> oxide layers are formed on RHEAs. Mo addition to a TiNbTa<sub>0.5</sub>Zr alloy resulted in an MoO<sub>3</sub> oxide layer being formed, and this layer was evaporated at high temperatures due to the drastic decrease in the oxidation resistance; the same alloy without Mo was found to have a high oxidation resistance. After a certain amount of time, the MoO<sub>3</sub> and Nb<sub>2</sub>O<sub>5</sub> oxide layers were found to evaporate. The CrTaO<sub>4</sub> oxide layer was found to have a higher oxidation resistance than the other oxide layers. The aluminizing technique is used in refractory high-entropy alloys to improve oxidation resistance.

An Hf<sub>0.5</sub>Nb<sub>0.5</sub>Ta<sub>0.5</sub>Ti<sub>1.5</sub>Zr refractory high-entropy alloy has a higher corrosion resistance than the previously reported RHEAs and 316L stainless steel. Ta added to the alloy plays a vital role in the formation of a highly immune passive film. A TiZrTaHfNb alloy has a higher pitting corrosion resistance, general corrosion resistance, and high biocompatibility than 316L and Ti<sub>6</sub>AlV. High-temperature-annealed materials have a high corrosion resistance.

CALPHAD modeling, ICME, MATLAB-based computational methods, CompuTherm, and the PanNb thermodynamic database have given satisfactory results in reference to experimental results. These simulation and modeling software packages expedite the design and advancement of existing RHEAs, as well as the invention of new RHEAs.

**Funding:** This research was funded by Ministry of Science and Technology of the Republic of China (Taiwan), under grant numbers MOST 107-2221-E-194-024-MY3 and MOST 109-2221-E-194-011-MY2.

**Conflicts of Interest:** The authors declare no conflict of interest.

## References

1. Senkov, O.N.; Wilks, G.B.; Miracle, D.B.; Chuang, C.P.; Liaw, P.K. Refractory high-entropy alloys. *J. Intermet.* **2010**, *18*, 1758–1765. [[CrossRef](#)]
2. Wu, S.J.; Wang, X.D.; Lu, J.T.; Qu, R.T.; Zhang, Z.F. Room-Temperature Mechanical Properties of  $V_{20}Nb_{20}Mo_{20}Ta_{20}W_{20}$  High-Entropy Alloy. *Adv. Eng. Mater.* **2018**, *20*, 1200028. [[CrossRef](#)]
3. Tong, C.J.; Chen, Y.L.; Yeh, J.W.; Lin, S.J.; Chen, S.K.; Shun, T.T.; Tsau, C.H.; Chang, S.Y. Microstructure characterization of  $Al_xCoCrCuFeNi$  high-entropy alloy system with multi principal elements. *Metall. Mater. Trans. A* **2005**, *36*, 881–893. [[CrossRef](#)]
4. Kang, B.; Lee, J.; Ryu, H.J.; Hong, S.H. Ultra-high strength WNbMoTaV high-entropy alloys with fine grain structure fabricated by powder metallurgical process. *Mater. Sci. Eng. A* **2018**, *712*, 616–624. [[CrossRef](#)]
5. Sobol', O. Structure and properties of high-entropy alloys based on refractory metals. *Mater. Today Proc.* **2020**, *30*, 736–741. [[CrossRef](#)]
6. Murty, B.S.; Yeh, J.W.; Ranganathan, S.; Bhattacharjee, P.P. Special subgroups of high-entropy alloys. In *High-Entropy Alloys*, 2nd ed.; Elsevier: Amsterdam, The Netherlands, 2019; pp. 145–163. [[CrossRef](#)]
7. Fu, A.; Guo, W.; Liu, B.; Cao, Y.; Xu, L.; Fang, Q.; Yang, H.; Liu, Y. A particle reinforced NbTaTiV refractory high entropy alloy-based composite with attractive mechanical properties. *J. Alloys Compd.* **2020**, *815*, 152466. [[CrossRef](#)]
8. Long, Y.; Su, K.; Zhang, J.; Liang, X.; Peng, H.; Li, X. Enhanced Strength of a Mechanical Alloyed NbMoTaWVTi Refractory High Entropy Alloy. *J. Mater.* **2018**, *11*, 669. [[CrossRef](#)]
9. Liu, Q.; Wang, G.; Sui, X.; Liu, Y.; Li, X.; Yang, J. Microstructure and mechanical properties of ultra-fine grained MoNbTaTiV refractory high-entropy alloy fabricated by spark plasma sintering. *J. Mater. Sci. Technol.* **2019**, *35*, 2600–2607. [[CrossRef](#)]
10. Kang, B.; Kong, T.; Raza, A.; Ryu, H.J.; Hong, S.H. Fabrication, microstructure and mechanical property of a novel Nb-rich refractory high-entropy alloy strengthened by in-situ formation of dispersoids. *Int. J. Refract. Hard Mater.* **2019**, *81*, 15–20. [[CrossRef](#)]
11. Dobbstein, H.; Thiele, M.; Gurevich, E.L.; George, E.P.; Ostendorf, A. Direct Metal Deposition of Refractory High Entropy Alloy MoNbTaW. *J. Phys. Procedia* **2016**, *83*, 624–633. [[CrossRef](#)]
12. Li, Q.; Zhang, H.; Li, D.; Chen, Z.; Huang, S.  $W_xNbMoTa$  Refractory High-Entropy Alloys Fabricated by Laser Cladding Deposition. *J. Mater.* **2019**, *12*, 533. [[CrossRef](#)] [[PubMed](#)]
13. Dobbstein, H.; Gurevich, E.L.; George, E.P.; Ostendorf, A.; Laplanche, G. Laser metal deposition of a refractory TiZrNbHfTa high-entropy alloy. *J. Addit. Manuf.* **2018**, *24*, 386–390. [[CrossRef](#)]
14. Dobbstein, H.; Gurevich, E.L.; George, E.P.; Ostendorf, A.; Laplanche, G. Laser metal deposition of compositionally graded TiZrNbTa refractory high-entropy alloys using elemental powder blends. *J. Addit. Manuf.* **2019**, *25*, 252–262. [[CrossRef](#)]
15. Sedegov, A.; Vorotilo, S.; Tsybullin, V.; Kuskov, K.; Moscovskikh, D. Synthesis and study of high-entropy ceramics based on the carbides of refractory metals. *IOP Conf. Ser. Mater. Sci. Eng.* **2019**, *588*, 012043. [[CrossRef](#)]
16. Melia, M.A.; Whetten, S.R.; Puckett, R.; Jones, M.; Heiden, M.J.; Argibay, N.; Kustas, A.B. High-throughput additive manufacturing and characterization of refractory high entropy alloys. *Appl. Mater. Today* **2020**, *19*, 100560. [[CrossRef](#)]
17. Xin, S.W.; Zhang, M.; Yang, T.T.; Zhao, Y.Y.; Sun, B.R.; Shen, T.D. Ultrahard bulk nanocrystalline VNbMoTaW high-entropy alloy. *J. Alloys Compd.* **2018**, *769*, 597–604. [[CrossRef](#)]
18. Yao, H.W.; Qiao, J.W.; Hawk, J.A.; Zhou, H.F.; Chen, M.W.; Gao, M.C. Mechanical properties of refractory high-entropy alloys: Experiments and modeling. *J. Alloys Compd.* **2017**, *696*, 1139–1150. [[CrossRef](#)]
19. Wang, G.; Liu, Q.; Yang, J.; Li, X.; Sui, X.; Gu, Y.; Liu, Y. Synthesis and thermal stability of a nanocrystalline MoNbTaTiV refractory high-entropy alloy via mechanical alloying. *Int. J. Refract. Met. Hard Mater.* **2019**, *84*, 104988. [[CrossRef](#)]
20. Senkov, O.N.; Scott, J.M.; Senkova, S.V.; Miracle, D.B.; Woodward, C.F. Microstructure and room temperature properties of a high-entropy TaNbHfZrTi alloy. *J. Alloys Compd.* **2011**, *509*, 6043–6048. [[CrossRef](#)]
21. Yang, C.; Aoyagi, K.; Bian, H.; Chiba, A. Microstructure evolution and mechanical property of a precipitation-strengthened refractory high-entropy alloy HfNbTaTiZr. *J. Mater. Lett.* **2019**, *254*, 46–49. [[CrossRef](#)]
22. Senkov, O.N.; Zhang, C.; Pilchak, A.L.; Payton, E.J.; Woodward, C.; Zhang, F. CALPHAD-aided development of quaternary multi-principal element refractory alloys based on NbTiZr. *J. Alloys Compd.* **2019**, *783*, 729–742. [[CrossRef](#)]
23. Fang, S.; Chen, W.; Fu, Z. Microstructure and mechanical properties of twinned  $Al_{0.5}CrFeNiCo_{0.3}C_{0.2}$  high entropy alloy processed by mechanical alloying and spark plasma sintering. *J. Mater. Des.* **2014**, *54*, 973–979. [[CrossRef](#)]
24. Fu, Z.; Chen, W.; Wen, H.; Morgan, S.; Chen, F.; Zheng, B.; Zhou, Y.; Zhang, L.; Lavernia, E.J. Microstructure and mechanical behavior of a novel  $Co_{20}Ni_{20}Fe_{20}Al_{20}Ti_{20}$  alloy fabricated by mechanical alloying and spark plasma sintering. *Mater. Sci. Eng. A* **2015**, *644*, 10–16. [[CrossRef](#)]
25. Lv, S.; Zu, Y.; Chen, G.; Fu, X.; Zhou, W. An ultra-high-strength CrMoNbWTi-C high entropy alloy co-strengthened by dispersed refractory IM and UHTC phases. *J. Alloys Compd.* **2018**, *788*, 1256–1264. [[CrossRef](#)]
26. Senkov, O.N.; Senkova, S.V.; Woodward, C. Effect of aluminum on two refractory high-entropy alloys' microstructure and properties. *Acta Mater.* **2014**, *68*, 214–228. [[CrossRef](#)]
27. Ley, N.A.; Sengovia, S.; Gorsse, S.; Young, M.L. Characterization and Modeling of NbNiTaTiW and NbNiTaTiW-Al Refractory High-Entropy Alloys. *Metall. Mater. Trans. A* **2019**, *50*, 4867–4876. [[CrossRef](#)]
28. Chang, S.; Tseng, K.-K.; Yang, T.-Y.; Chao, D.-S.; Yeh, J.-W.; Liang, J.-H. Irradiation-induced swelling and hardening in HfNbTaTiZr refractory high entropy alloy. *Mater. Lett.* **2020**, *272*, 127832. [[CrossRef](#)]

29. Yurchenko, N.; Panina, E.; Tikhonovsky, M.; Salishchev, G.; Zhrebtsov, S.; Stepanov, N. Structure and mechanical properties of an in situ refractory  $\text{Al}_{20}\text{Cr}_{10}\text{Nb}_{15}\text{Ti}_{20}\text{V}_{25}\text{Zr}_{10}$  high entropy alloy composite. *Mater. Lett.* **2020**, *264*, 127372. [[CrossRef](#)]
30. Xiang, L.; Guo, W.; Liu, B.; Fu, A.; Li, J.; Fang, Q.; Liu, Y. Microstructure and Mechanical Properties of TaNbVTiAl<sub>x</sub> Refractory High-Entropy Alloys. *Entropy* **2020**, *3*, 282. [[CrossRef](#)]
31. Guo, W.; Liu, B.; Liu, Y.; Li, T.; Fu, A.; Fang, Q.; Nie, Y. Microstructures and mechanical properties of ductile NbTaTiV refractory high entropy alloy prepared by powder metallurgy. *J. Alloys Compd.* **2019**, *776*, 428–436. [[CrossRef](#)]
32. Zhu, M.; Yao, L.; Liu, Y.; Zhang, M.; Li, K.; Jian, Z. Microstructure evolution and mechanical properties of a novel CrNbTiZrAl<sub>x</sub> ( $0.25 < x < 1.25$ ) eutectic refractory high-entropy alloy. *Mater. Lett.* **2020**, *272*, 127869. [[CrossRef](#)]
33. Han, Z.D.; Luan, H.W.; Liu, X.; Chen, N.; Li, X.Y.; Shao, Y.; Yao, K.F. Microstructures and mechanical properties of Ti<sub>x</sub>NbMoTaW refractory high-entropy alloys. *Mater. Sci. Eng. A* **2017**, *712*, 380–385. [[CrossRef](#)]
34. Matsuno, H.; Yokoyama, A.; Watari, F.; Uo, M.; Kawasaki, T. Biocompatibility and osteogenesis of refractory metal implants, titanium, hafnium, Niobium, tantalum, and rhenium. *Biomaterials* **2011**, *22*, 1253–1262. [[CrossRef](#)]
35. Pandey, P.; Sawant, A.K.; Nithin, B.; Peng, Z.; Makineni, S.K.; Gault, B.; Chattopadhyay, K. On the effect of Re addition on microstructural evolution of a CoNi-based superalloy. *Acta Mater.* **2019**, *168*, 37–51. [[CrossRef](#)]
36. Yusenko, K.; Riva, S.; Carvalho, P.A.; Yusenko, M.V.; Arnaboldi, S.; Sheik, A.S.; Hanfland, M.; Gromilov, S.A. First hexagonal close-packed high-entropy alloy with outstanding stability under extreme conditions and electrocatalytic activity for methanol oxidation. *Scr. Mater.* **2017**, *138*, 22–27. [[CrossRef](#)]
37. Yan, D.; Song, K.; Sun, H.; Wu, S.; Zhang, H.; Yuan, S.; Kim, J.T.; Chawake, N.; Renk, O.; Hohenwarter, A.; et al. Microstructures, Mechanical Properties, and Corrosion Behaviors of Refractory High-Entropy ReTaWNbMo Alloys. *J. Mater. Eng. Perform.* **2019**, *29*, 399–409. [[CrossRef](#)]
38. Whitfield, T.E.; Pickering, E.J.; Talbot, C.E.; Jones, C.N.; Stone, H.J.; Jones, N.G. Observation of a refractory metal matrix containing Zr-Ti-rich precipitates Mo<sub>0.5</sub>NbTa<sub>0.5</sub>TiZr high entropy alloy. *Scr. Mater.* **2020**, *180*, 71–76. [[CrossRef](#)]
39. Panina, E.S.; Yurchenko, N.Y.; Zhrebtsov, S.V.; Tikhonovsky, M.A.; Mishunin, N.; Stepanov, D. Structures and mechanical properties Ti-Nb-Cr-V-Ni-Al refractory high entropy alloys. *Mater. Sci. Eng. A* **2020**, *786*, 139409. [[CrossRef](#)]
40. Senkov, O.N.; Wilks, G.B.; Scott, J.M.; Miracle, D.B. Mechanical properties of Nb<sub>25</sub>Mo<sub>25</sub>Ta<sub>25</sub>W<sub>25</sub> and V<sub>20</sub>Nb<sub>20</sub>Mo<sub>20</sub>Ta<sub>20</sub>W<sub>20</sub> refractory high entropy alloys. *Intermetallics* **2011**, *19*, 698–706. [[CrossRef](#)]
41. Wang, M.; Ma, Z.; Xu, Z.; Cheng, X. Microstructures and mechanical properties of HfNbTaTiZrW and HfNbTaTiZrMoW refractory high-entropy alloys. *J. Alloys Compd.* **2019**, *803*, 778–785. [[CrossRef](#)]
42. Shafiei, A. A new approach to model the yield strength of body-centered cubic solid solution refractory high-entropy alloys. *Tungsten* **2020**, *2*, 307–320. [[CrossRef](#)]
43. Ge, S.; Fu, H.; Zhang, L.; Mao, H.; Li, H.; Wang, A.; Li, W.; Zhang, H. Effects of Al addition on the microstructures and properties of MoNbTaTiV refractory high entropy alloy. *Mater. Sci. Eng. A* **2020**, *784*, 139275. [[CrossRef](#)]
44. Long, Y.; Liang, X.; Su, K.; Peng, H.; Li, X. A fine-grained NbMoTaWVCr refractory high-entropy alloy with ultra-high-strength: Microstructural evolution and mechanical properties. *J. Alloys Compd.* **2019**, *780*, 607–617. [[CrossRef](#)]
45. Moschetti, M.; Xu, A.; Schuh, B.; Hohenwarter, A.; Couzinie, J. On the Room-Temperature Mechanical Properties of an Ion-Irradiated TiZrNbHfTa Refractory High Entropy Alloy. *JOM* **2020**, *72*, 130–138. [[CrossRef](#)]
46. Xu, Z.; Ma, Z.; Wang, M.; Chen, Y.; Tan, Y.; Cheng, X. Design of novel low-density refractory high entropy alloys for high-temperature applications. *Mater. Sci. Eng. A* **2019**, *755*, 318–322. [[CrossRef](#)]
47. Senkov, O.N.; Couzinie, J.P.; Rao, S.I.; Soni, V.; Banerjee, R. Temperature-dependent deformation behavior and strengthening mechanisms in a low density refractory high entropy alloy Al<sub>10</sub>Nb<sub>15</sub>Ta<sub>5</sub>Ti<sub>30</sub>Zr<sub>40</sub>. *Materialia* **2020**, *9*, 100627. [[CrossRef](#)]
48. Sadeghilaridjani, M.; Muskeri, S.; Hassannaemi, V.; Pole, M.; Mukherjee, S. Strain rate sensitivity of a novel refractory high entropy alloy: Intrinsic versus extrinsic effects. *Mater. Sci. Eng. A* **2019**, *766*, 138326. [[CrossRef](#)]
49. Ma, Y.; Wu, S.; Jia, Y.; Hu, P.; Bu, Y.; Chen, X.; Wang, G.; Liu, J.; Wang, H.; Zhai, Q. Hexagonal Closed-Packed Precipitation Enhancement in a NbTiHfZr Refractory High-Entropy Alloy. *Metals* **2019**, *9*, 485. [[CrossRef](#)]
50. Wei, Q.; Shen, Q.; Zhang, J.; Zhang, Y.; Luo, G.; Zhang, L. Microstructure evolution, mechanical properties, and strengthening mechanism of refractory high-entropy alloy matrix composites with the addition of TaC. *J. Alloys Compd.* **2019**, *777*, 1168–1175. [[CrossRef](#)]
51. Cao, Y.; Liu, Y.; Li, Y.; Liu, B.; Wang, J.; Du, M.; Liu, R. Precipitation strengthening in a hot-worked TiNbTa<sub>0.5</sub>ZrAl<sub>0.5</sub> refractory high entropy alloy. *Mater. Lett.* **2019**, *246*, 186–189. [[CrossRef](#)]
52. Roh, A.; Kim, D.; Nam, S.; Kim, D.I.; Kim, H.Y.; Lee, K.A.; Choi, H.; Kim, J.H. NbMoTaW refractory high entropy alloy composites strengthened by in-situ metal-non-metal compounds. *J. Alloys Compd.* **2020**, *822*, 153423. [[CrossRef](#)]
53. Chen, S.; Tseng, K.K.; Tong, Y.; Li, W.; Yeh, C.W.; Liaw, P.K. Grain growth and Hall-Petch relationship in a refractory HfNbTaZrTi high-entropy alloy. *J. Alloys Compd.* **2019**, *795*, 19–26. [[CrossRef](#)]
54. Eleti, R.R.; Chokshi, A.H.; Shibata, A.; Tsuji, N. Unique high-temperature deformation dominated by grain boundary sliding in a heterogeneous necklace structure formed by dynamic recrystallization in HfNbTaTiZr BCC refractory high entropy alloy. *Acta Mater.* **2020**, *183*, 64–77. [[CrossRef](#)]
55. Yurchenko, N.Y.; Panina, E.S.; Zhrebtsov, S.V.; Tikhonovsky, M.A.; Salishchev, G.A.; Stepanov, N.D. Microstructure evolution of a novel low-density Ti-Cr-Nb-V refractory high entropy alloy during cold rolling and subsequent annealing. *Mater. Charact.* **2019**, *158*, 109980. [[CrossRef](#)]

56. Zhrebtsov, S.; Yurchenko, N.; Tikhonovsky, M.; Stepanov, N.D. Microstructure and Mechanical Properties Evolution in HfNbTa-TiZr Refractory High Entropy Alloy During Cold Rolling. *Adv. Eng. Mater.* **2020**, *22*, 2000105. [[CrossRef](#)]
57. Panina, E.; Yurchenko, N.; Zhrebtsov, S.; Stepanov, N.; Salishchev, G.; Ventzke, V.; Dinse, R.; Kashaev, N. Laser Beam Welding of a Low-Density Refractory. *Metals* **2019**, *9*, 1351. [[CrossRef](#)]
58. Kim, H.; Nam, S.; Roh, A.; Son, M.; Ham, M.H.; Kim, J.H.; Choi, H. Mechanical and electrical properties of NbMoTaW refractory high-entropy alloy thin films. *Int. J. Refract. Met. Hard Mater.* **2019**, *80*, 286–291. [[CrossRef](#)]
59. Tunes, M.A.; Vishnyakov, V.M. Microstructural origins of the high mechanical damage tolerance of NbTaMoW refractory high-entropy alloy thin films. *Mater. Des.* **2019**, *170*, 107692. [[CrossRef](#)]
60. Wang, H.; Liu, Q.; Guo, Y.; Lan, H. MoFe<sub>1.5</sub>CrTiWAlNb<sub>x</sub> refractory high-entropy alloy coating fabricated by laser cladding. *Intermetallics* **2019**, *115*, 106613. [[CrossRef](#)]
61. Guo, Y.; Wang, H.; Liu, Q. Microstructure evolution and strengthening mechanism of laser-cladding MoFexCrTiWAlNb<sub>y</sub> refractory high-entropy alloy coatings. *J. Alloys Compd.* **2020**, *834*, 155147. [[CrossRef](#)]
62. Cao, Y.K.; Liu, Y.; Liu, B.; Zhang, W.D.; Du, M. Effects of Al and Mo on the high-temperature oxidation behavior of refractory high entropy alloys. *Trans. Nonferrous Metals Soc. China* **2019**, *29*, 1476–1483. [[CrossRef](#)]
63. Waseem, O.A.; Ryu, H.J. Combinatorial synthesis and analysis of Al<sub>x</sub>Ta<sub>y</sub>V<sub>z</sub>-Cr<sub>20</sub>Mo<sub>20</sub>Nb<sub>20</sub>Ti<sub>20</sub>Zr<sub>10</sub> Al<sub>10</sub>CrMo<sub>x</sub>NbTiZr<sub>10</sub> refractory high-entropy alloys: Oxidation behavior. *J. Alloys Compd.* **2020**, *828*, 154427. [[CrossRef](#)]
64. Butler, T.M.; Chaput, K.J. Native oxidation resistance of Al<sub>20</sub>Nb<sub>30</sub>Ta<sub>10</sub>Ti<sub>30</sub>Zr<sub>10</sub> refractory complex concentrated alloy (RCCA). *J. Alloys Compd.* **2019**, *787*, 606–617. [[CrossRef](#)]
65. Müller, F.; Gorr, B.; Christ, H.-J.; Müller, J.; Butz, B.; Chen, H.; Kauffmann, A.; Heilmaier, M. On the oxidation mechanism of refractory high entropy alloys. *Corros. Sci.* **2019**, *159*, 108161. [[CrossRef](#)]
66. Gorr, B.; Müller, F.; Schellert, S.; Christ, H.-J.; Chen, H.; Kauffmann, A.; Heilmaier, M. A new strategy to intrinsically protect refractory metal-based alloys at ultra-high temperatures. *Corros. Sci.* **2020**, *166*, 108475. [[CrossRef](#)]
67. Lo, K.; Murakami, H.; Yeh, J.; Yeh, A. Intermetallics Oxidation behavior of a novel refractory high entropy alloy at elevated temperatures. *Intermetallics* **2020**, *119*, 106711. [[CrossRef](#)]
68. Zhang, P.; Li, Y.; Chen, Z.; Zhang, J.; Shen, B. Oxidation response of a vacuum arc melted NbZrTiCrAl refractory high entropy alloy at 800–1200 °C. *Vacuum* **2019**, *162*, 20–27. [[CrossRef](#)]
69. Sheikh, S.; Gan, L.; Tsao, Y.K.; Murakami, H.; Shafeie, S.; Guo, S. Aluminizing for enhanced oxidation resistance of ductile refractory high-entropy alloys. *Intermetallics* **2018**, *103*, 40–51. [[CrossRef](#)]
70. Sheikh, S.; Gan, L.; Montero, X.; Murakami, H.; Guo, S. Forming a protective alumina scale for ductile refractory high-entropy alloys via aluminizing. *Intermetallics* **2020**, *123*, 106838. [[CrossRef](#)]
71. Zhou, Q.; Sheikh, S.; Ou, P.; Chen, D.; Hu, Q.; Guo, S. Corrosion behavior of Hf<sub>0.5</sub>Nb<sub>0.5</sub>Ta<sub>0.5</sub>Ti<sub>1.5</sub>Zr refractory high-entropy in aqueous chloride solutions. *Electrochem. Commun.* **2019**, *98*, 63–68. [[CrossRef](#)]
72. Motallebzadeh, A.; Peighambaroust, N.S.; Sheikh, S.; Murakami, H.; Guo, S.; Canadinc, D. Microstructural, mechanical, and electrochemical characterization of TiZrTaHfNb and Ti<sub>1.5</sub>ZrTa<sub>0.5</sub>Hf<sub>0.5</sub>Nb<sub>0.5</sub> refractory high-entropy alloys for biomedical applications. *Intermetallics* **2019**, *113*, 106572. [[CrossRef](#)]
73. Raturi, A.; Jaya Aditya, C.; Gurao, N.P.; Biswas, K. ICME approach to explore equiatomic and non-equiatomic single-phase BCC refractory high entropy alloys. *J. Alloys Compd.* **2019**, *806*, 587–595. [[CrossRef](#)]
74. Hu, Y.L.; Bai, L.H.; Deng, D.Y.; Liang, X.B.; Liang, X.B.; Zhang, J.; Li, Y.J.; Chen, Y.X. First-principle calculation investigation of NbMoTaW based refractory high entropy alloys. *J. Alloys Compd.* **2020**, *827*, 153963. [[CrossRef](#)]
75. Ishibashi, S.; Ikeda, Y.; Körmann, F.; Grabowski, B.; Neugebauer, J. Correlation analysis of strongly fluctuating atomic volumes, charges, and stresses in body-centered cubic refractory high-entropy alloys. *Phys. Rev. Mater.* **2020**, *4*, 023608. [[CrossRef](#)]